Photodynamic Control of Bioactivity in a Nanofiber Matrix

Shantanu Sur,[⊥,¶] John B. Matson,[⊥,#,¶] Matthew J. Webber,[§] Christina J. Newcomb,[†] and Samuel I. Stupp[⊥,†,‡,∥,*]

Departments of [†]Materials Science and Engineering, [‡]Chemistry, and [§]Biomedical Engineering, Northwestern University, Evanston, Illinois 60208, United States and [⊥]Institute for BioNanotechnology in Medicine and [∥]Department of Medicine, Northwestern University, Chicago, Illinois 60611, United States. [¶]These authors contributed equally to this work. [#]Present address: Department of Chemistry, Virginia Tech, Blacksburg, VA 24061.

ABSTRACT Self-assembling peptide materials have been used extensively to mimic natural extracellular matrices (ECMs) by presenting bioactive epitopes on a synthetic matrix. Although this approach can facilitate a desired response from cells grown in the matrix, it lacks the capacity for spatial or temporal regulation of the presented signals. We describe here a photoresponsive, synthetic ECM using a supramolecular platform composed of peptide amphiphiles (PAs) that self-assemble into cylindrical nanofibers. A photocleavable nitrobenzyl ester group was included in the peptide backbone using a novel Fmoc-amino acid that is compatible with microwave-assisted solid-phase peptide synthesis. The placement of the photolabile group on the peptide backbone enabled efficient removal of the ECM-derived cell adhesion epitope RGDS from PA molecules upon exposure to light (half-life of photolysis ~1.9 min) without affecting the nanofiber assembly. Fibroblasts cultured on RGDS-presenting PA nanofiber substrates demonstrated increased cell spreading and more mature focal adhesions compared with unfunctionalized and control (RGES-presenting) surfaces, as determined by immunostaining and cell morphological analysis. Furthermore, we observed an arrest in fibroblast spreading on substrates containing a cleavable RGDS epitope when the culture was exposed to light; in contrast, this dynamic shift in cell response was absent when the RGDS epitope was attached to the PA molecule by a light-insensitive control linker. Light-responsive bioactive materials can contribute to the development of synthetic systems that more closely mimic the dynamic nature of native ECM.
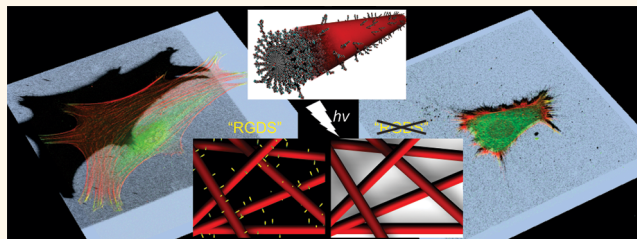
KEYWORDS: supramolecular nanofibers · cell morphological analysis · nitrobenzyl · projected cell area · photodegradable · RGDS epitope

The extracellular matrix (ECM) forms a supporting structure around cells and plays a critical role in cell development, maturation, and repair by providing essential biochemical and biophysical cues.[1] To provide cells with the necessary signals at the right time and place, the ECM is known to undergo extensive remodeling during these processes.[1,2] The ability to change spatiotemporal composition of the ECM allows certain amphibian species to regenerate entire organs and limbs, where specific ECM components guide the developmental steps of regenerating cells by providing necessary instructive cues.[3] This observation raises the possibility that complex regeneration in higher mammalian species can also be accomplished by providing an appropriate sequence of signals in the extracellular environment. Since the discovery of short, bioactive peptide sequences in native ECM molecules,[4,5]

incorporation of peptide epitopes in artificial synthetic matrices has become a general strategy to impart biofunctionality to an otherwise inert material.[6−9] For example, the display of the laminin-derived IKVAV epitope on a synthetic scaffold has been shown to direct the differentiation of neural progenitor cells into neurons and control the survival and maturation of differentiated neurons.[9,10] One important need in the development of highly functional ECM mimetic materials is the capacity for *dynamic* signaling, a process used in native ECM to deliver specific signals at distinct stages of cellular development and maturation.[11] Synthetic dynamic matrices could be designed to allow for similar changes, ideally through the use of convenient external stimuli with spatial and temporal control, allowing for precise tuning of the cellular environment.[12] Spatiotemporal control of signaling epitopes in dynamic scaffolds

could more effectively direct cell function, for example, in proliferation and differentiation of stem cells for regenerative therapies.[11,13] Additionally, dynamic matrices would allow researchers to study the effects of specific matrix modifications over time and space *in vitro*, reducing the inherent difficulty and complexity of studying cellular processes *in vivo*.

Development of dynamic matrices for regenerative medicine requires materials capable of forming robust, viscoelastic gels that are amenable to cell encapsulation and support cell viability. Self-assembling peptides have been extensively studied as bioactive gels for cell culture.[14−18] These peptidic supramolecular materials have several advantages over traditional polymer hydrogels, including dense signaling capacity, the absence of toxic cross-linking agents, inherent biocompatibility and biodegradation, sheer-thinning behavior or *in vivo* gelation, and facile chemical modification.[12] A very broad family of such materials has been developed and investigated by our group, known as peptide amphiphiles (PAs).[8,19] PAs contain peptide sequences covalently connected to hydrophobic segments such as alkyl tails.[20] When the peptide component contains residues with propensity for β-sheet formation, spontaneous self-assembly of PAs in aqueous media leads to the formation of filamentous assemblies of molecules that resemble the fibrous structures in native ECM.[8,21] PA nanofibers are capable of presenting ECM-derived epitopes, such as RGD and IKVAV, at a very high density,[8,9] and the density of epitopes can be tuned for optimal signaling.[22,23] Our group has investigated the ability of PA nanofibers to signal cells in a broad platform that includes cardiovascular disease targets,[24,25] central and peripheral nervous system repair,[9,26−28] drug delivery,[29−34] cancer therapeutics,[32,35] as well as bone,[36,37] cartilage,[38] and enamel regeneration.[39] Extension of the well-established signaling capacity of PAs to systems with dynamic signaling capacity would greatly expand the possibilities of self-assembling peptide materials for controllable and tunable regenerative therapies.

One possible feature to incorporate dynamic signaling into PA matrices is a chemical trigger that can be externally activated. The requirements for maintenance of cell viability (physiological pH and temperature, sterility, minimal shear stress, benign chemistry, among others) severely limit the possibilities for this trigger. Another prospect is the use of enzymes, a technique which has been studied in the context of initiating self-assembly by our group and others.[31,40,41] Chemically degradable bonds such as disulfides can also be used with an external stimulus (*e.g.*, a reducing agent) to trigger a change in gel properties.[42] The simplest trigger that is an orthogonal stimulus to biological processes and offers a high degree of spatial and temporal control is light, provided that the intensity and duration of exposure are sufficiently low.
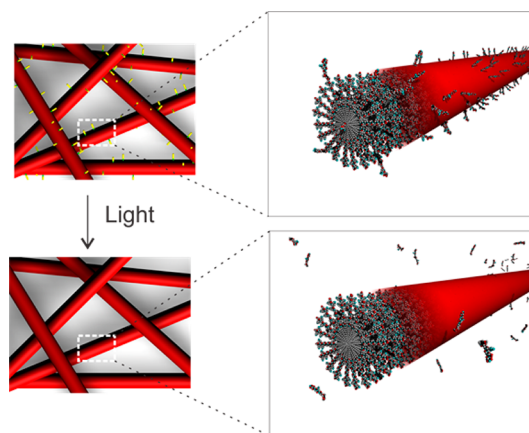

Figure 1. Schematic representation of epitope removal from PA nanofiber surfaces following exposure to light.

Recognizing this possibility, we previously employed light-mediated processes to alter the assembly state of PAs.[43,44] In one case, the bioactivity of an appended epitope was shown to increase as the PA assembly shifted from spherical micelles to cylindrical nanofibers through the light-triggered reorganization of the supramolecular assembly.[44] In other recent work, Shoichet used photochemical deprotection of thiols in agarose matrices for protein conjugation,[45] and Anseth found 365 nm UV light, used under controlled intensity and exposure, to be a suitable stimulus for matrix or epitope removal in a light-sensitive PEG-acrylate-based hydrogel system.[13,46] Matrices developed by Anseth have been used to promote chondrogenic differentiation of human mesenchymal stem cells through temporal changes in epitope presentation. Inspired by these previous systems, we hoped to develop a self-assembling PA that retained its capacity for supramolecular nanofiber formation with the added capacity for light-mediated dynamics in a regulated temporal and/or spatial profile (Figure 1). Such a material would extend the scope of light-responsive matrices to include self-assembled gels, which would retain all of the advantages over cross-linked polymer hydrogels noted above in addition to the added capacity of light-regulated changes. We report here the design of light-responsive PA nanofibers using a new photolabile Fmoc-amino acid compared with a similar photostable control molecule. To evaluate the light-induced dynamic epitope regulation in these self-assembled nanofibers, an integrin-binding RGDS peptide sequence was incorporated in the PA molecule and compared with a mutated RGES epitope. The effects of light-induced epitope removal were assessed by fibroblast spreading measurements and focal adhesion formation on the nanofiber matrices.

RESULTS AND DISCUSSION

Synthesis and Characterization of Light-Responsive PA. For incorporation of a photolabile group into the peptide sequence, we designed Fmoc-amino acid **I** (Figure 2,
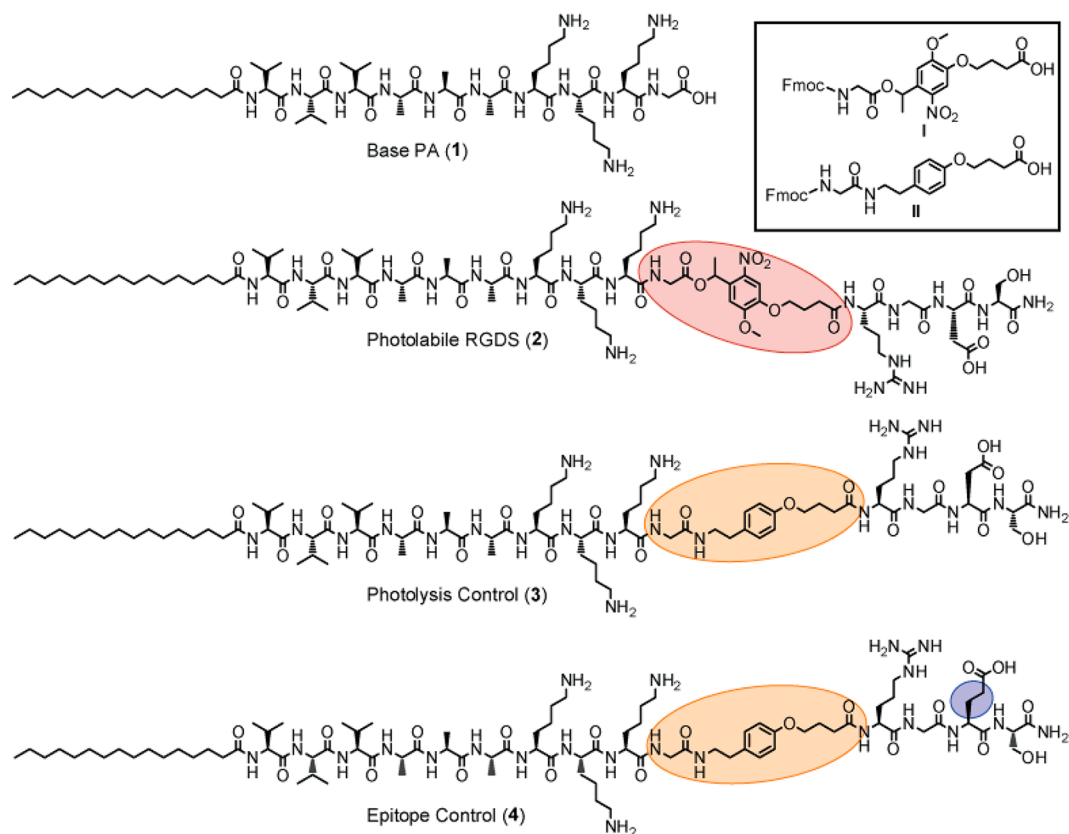
Figure 2. Chemical structures of PAs used in this study with highlighted regions of significance. PA 1 is the base sequence. PA 2 contains a photolabile linker (red oval) and the RGDS cell adhesion sequence; PA 3 contains a control, nonphotolabile linker (orange oval) and the RGDS sequence, while PA 4 contains the same nonphotolabile linker and a mutated RGES sequence (blue oval). Inset: Chemical structures of photocleavable Fmoc-amino acid I and nonphotocleavable control Fmoc-amino acid II (synthetic details available in Supporting Information).

inset). The design employs a nitrobenzyl ester as the photocleavable component, similar to other photocleavable units in the literature.[47−51] To create an Fmoc-amino acid that can be used in solid-phase peptide synthesis (SPPS) like any standard amino acid, an Fmoc-protected glycine residue was also incorporated into amino acid I (see Supporting Information for synthetic details). Additionally, as a control molecule that had a similar chemical structure but lacked the capacity for cleavage under UV light, Fmoc-amino acid II was designed and synthesized.[52] The strength of this approach is that the photolabile component (I) and the control (II) have similar chemical functionalities and are similar in size. Usage of I and II in comparison studies therefore allows for direct control over the variable of photostability with minimal effects on other aspects of the peptide, such as total backbone length. Fmoc-amino acids I and II were both found to be compatible with SPPS on a microwave-assisted peptide synthesizer and in manual SPPS. Couplings were carried out with HBTU and DIEA, and the amino acids were stable to cleavage with 95% TFA.

Our strategy to investigate cellular response to a dynamic change in the bioactivity of a matrix was to synthesize a group of PAs bearing the RGDS peptide sequence (Figure 2). The fibronectin-derived RGDS epitope was chosen for its well-known role in mediating cell adhesion and its consequent relevance in the design of bioactive biomaterials.[6] All PAs were designed from a common base sequence of PA 1, $C_{16}V_3A_3K_3G$ (where C_{16} = palmitic acid), a design similar to PAs commonly used in our laboratory.[53] PA 2 incorporates in its sequence photolabile amino acid residue I between the base sequence and the RGDS epitope. This PA serves as the bioactive and photolabile molecule in our study. PA 3 was designed as a control for the photocleavable component and contains the nonphotolabile amino acid II residue and the bioactive RGDS epitope. PA 4 is a nonphotolabile control molecule for the bioactive peptide, containing the mutated epitope RGES. All PAs were synthesized using standard SPPS conditions and purified by HPLC.

The PAs were characterized by cryogenic transmission electron microscopy (cryoTEM) and small-angle X-ray scattering (SAXS) to study their supramolecular architecture. All PAs show cylindrical nanofiber formation by cryoTEM, and SAXS data support these observations (Figure S2 in the Supporting Information). Figure 3 shows the cryoTEM images for PAs 1−4, including PA 2 before and after photolysis at 365 nm
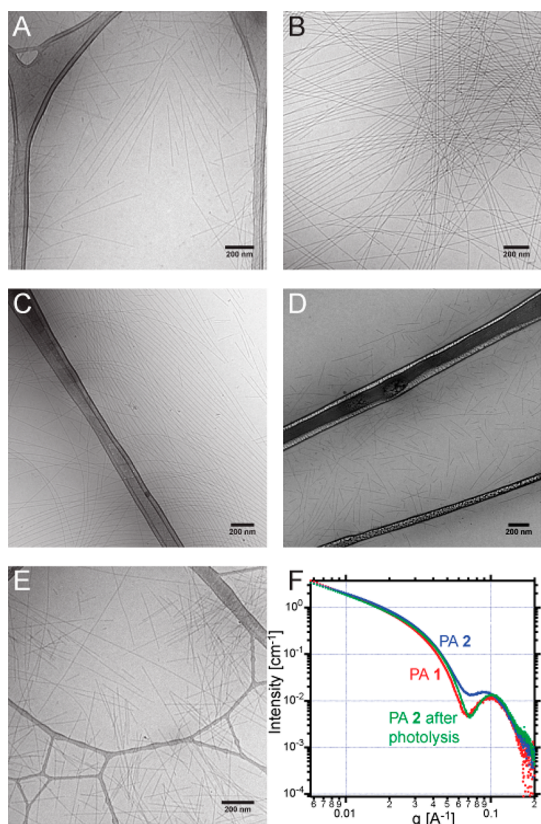
Figure 3. CryoTEM (A—E) and SAXS (F) in H$_2$O of PAs used in this study. CryoTEM images of PA 1 (A), PA 2 without irradiation (B), PA 2 after irradiation (C), PA 3 (D), and PA 4 (E) all show cylindrical nanofiber morphologies. SAXS curves of PAs 1, 2, and 2 after photolysis (F) indicate that the dimensions of self-assembled nanofibers of PA 2 after irradiation become the same as that observed for PA 1.

Figure 4. (A,B) Conventional TEM images showing (A) streptavidin-tagged AuNPs selectively bound to the surface of biotin-containing PA 5 nanofibers (arrows point to AuNPs), and (B) streptavidin-tagged AuNPs mixed with PA 5 after irradiation showing no specific binding. (C) Kinetics of photolysis measured using PA 5 (blue data points) with fitting of the data (black line) to first-order kinetics ($t_{1/2}$ = 1.9 min).

in a Rayonet photoreactor (9.5 mW/cm^2) for 10 min. High aspect ratio nanofibers are observed in all cases by cryoTEM, indicating that neither the addition of the photolabile or nonphotolabile amino acid residues nor the irradiation has an effect on their supramolecular structure. We also used SAXS to confirm our observations by TEM and more precisely analyze fiber dimensions. The SAXS data in Figure 3F show the curves corresponding to PA 2 before and after irradiation as well as that of PA 1. PA 2 generates PA 1 upon photolytic removal of the RGDS portion of the sequence, and the scattering curve of PA 2 after irradiation is almost the same as that of an authentic sample of PA 1. We attribute the slight differences in authentic PA 1 and irradiated PA 2 to a change in the scattering length density of the solvent as it absorbs the cleaved RGDS sequence. The fitting of the SAXS data to a core—shell cylinder model yields nanofiber diameters of 8.4 nm for PA 1, 9.7 nm for PA 2 before irradiation, and 8.0 nm for PA 2 after irradiation (Table S1).

Epitope Accessibility and Photolysis Kinetics. A successful design of a dynamic scaffold using photoresponsive PA molecules will not only require efficient removal of epitopes upon light treatment, but the epitopes should
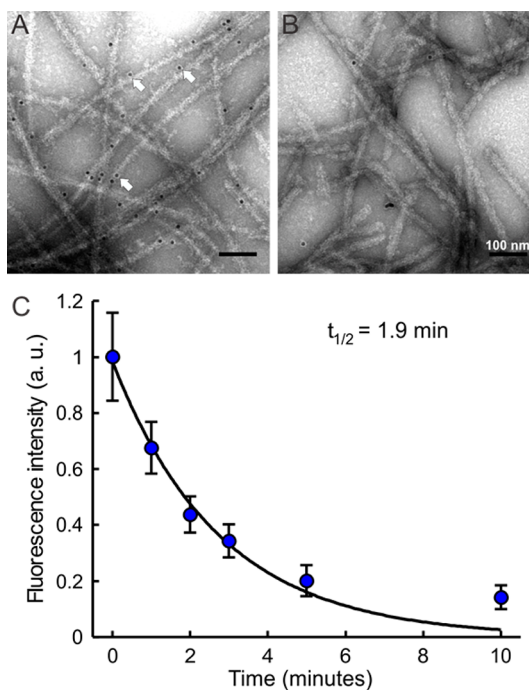
also be accessible to cells to serve their intended function prior to irradiation. To test the accessibility of the epitopes when presented adjacent to the photolabile segment, a biotin-containing photolabile PA was synthesized using Fmoc-amino acid I (PA 5; structure shown in Supporting Information, Figure S1). Nanofibers formed by this PA were incubated with streptavidin-conjugated 10 nm gold nanoparticles (AuNPs) and observed under TEM. The AuNPs were predominantly distributed along the nanofibers (Figure 4A), indicating specific binding of streptavidin to the biotin groups displayed on the nanofiber surfaces. The binding was strongly reduced if the biotin was removed by PA irradiation before addition of the AuNPs (Figure 4B).

To evaluate the kinetics of photolysis, we used a fluorescence-based approach using the same biotin-presenting PA 5. The PA was coated on glass coverslips for this measurement to keep consistency with the methods described in subsequent cell experiments. To generate a consistent and strongly adhered PA coating, coverslips were first treated with positively charged poly-D-lysine, followed by negatively charged, non-adherent alginate, followed last by positively charged PA nanofibers (Figure S3). PA-coated coverslips were then irradiated for specific time intervals, and at each time point, the photoirradiated coverslips were washed to remove cleaved biotin and then incubated with AlexaFluor-488-tagged streptavidin.
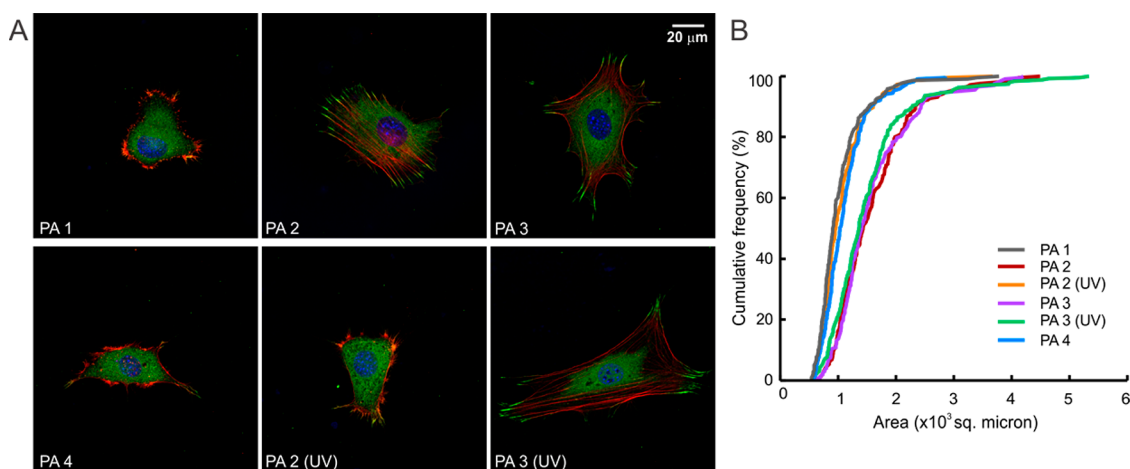
Figure 5. Cell response to photoresponsive PA and controls. (A) Representative morphologies of 3T3 fibroblasts on various PA-coated surfaces (with or without UV exposure). Staining for actin (phalloidin, red) and vinculin (green) reveals the cytoskeletal organization and focal adhesions, respectively. **(B)** Cumulative distribution plot of projected cell surface area, where each point represents the total percentage of cells smaller than the given area. The data show an increased cell spreading in the presence of RGDS epitopes (PAs 2, 3, and 3 (UV)); this response was absent when the epitopes were not included or removed by photoirradiation (PAs 1, 2 (UV), and 4).

The fluorescence intensity measured from the coverslips after irradiation indicated the quantity of remaining biotin groups on the PA-coated surface. The data show an exponential decay consistent with first-order kinetics, with a photolysis half-life of 1.9 min (Figure 4C).

Cell Adhesion and Morphological Analysis. Since fibroblast cell response to RGD epitopes presented on material surfaces has been extensively studied,[22,54−56] we selected mouse 3T3 fibroblasts for our experiments. Adhesion and spreading of cells have been shown to be dependent on RGDS epitope density and spacing.[55−57] In order to space out RGDS epitopes on the nanofiber surface, we used epitope-presenting PAs **2**, **3**, and **4** as binary mixtures with the base PA **1**. PA mixtures were generated by lyophilizing PA solutions from hexafluoroisopropanol (HFIP), as previously reported by our group.[29,32] The mixed PA powders were then dissolved in water and coated onto glass coverslips as described above. The intermediate alginate layer in the coating not only helped to form a stable PA coating, but its poor cell attachment properties also reduced the possibility of any confounding observations that may arise from cellular attachment to underlying glass or poly-D-lysine coatings. Our group and others have found that mixtures consisting of 10% epitope-presenting peptide and 90% base peptide are optimal for cell response.[22,23,58] Our preliminary experiments also showed increased fibroblast spreading on PA coatings consisting of 10% RGDS epitope-presenting PA (PA **2**) mixed with 90% base PA **1** compared with a pure PA **1** coating. The extent of enhancement was reduced when the proportion of RGDS-presenting PA was increased to 20% (Figure S3). On the basis of these results, all further experiments were run using a 90:10 ratio of base PA (PA **1**) to epitope-presenting PA.

We evaluated the cell response to PAs using serum-free culture media in order to limit nonspecific adsorption of proteins to the nanofiber surface.[54] When plated on PA-coated surfaces, fibroblasts showed attachment regardless of the presence or absence of RGDS epitopes. It should be noted that attachment is distinct from adhesion. The former describes any form of cell immobilization on a surface, while the latter implies cell interaction with a surface through specific receptor proteins such as integrins. The lack of epitope specificity and the fast time scale (<30 min) of this initial attachment suggests that it is driven by electrostatic interactions between the negatively charged cell surface and the positively charged nanofibers coupled with the innate property of peptide fibers to support cell attachment.[59] In the presence of RGDS epitopes (PA **2** and PA **3**), however, we observed a higher degree of cell spreading after 5 h incubation time associated with a frequent polygonal cell shape (Figure 5A and Figure S3). In the absence of the epitope (PA **1**) or in presence of the nonbioactive RGES epitope (PA **4**), spreading was severely restricted and cells retained a circular contour. Vinculin, a protein marker for focal adhesions, was visualized by immunostaining and revealed localized expression near the periphery of polygonal cells, which provides anchorage to the substrate and facilitates the organization of the actin cytoskeleton. Round fibroblasts on surfaces of PAs **1** and **4**, however, rarely showed focal adhesions, and the organization of the actin cytoskeleton was also less distinct. Together these observations suggest that RGDS epitopes presented by the PA nanofibers play a crucial role in recruiting focal adhesion proteins, a process which favors cell spreading and attainment of a polygonal morphology.

To quantify our observations of cell morphology, measurements of projected cell surface area, convex

TABLE 1. Summary of Fibroblast Morphology Observed on Various PA-Coated Surfaces[a]

	PA 2		PA 3		PA 4	PA 1
UV exposure	no ($n = 205$)	yes ($n = 224$)	no ($n = 202$)	yes ($n = 236$)	no ($n = 217$)	no ($n = 218$)
area[b]	1601 ± 48***	1073 ± 28[n.s.]	1595 ± 49***	1514 ± 49***	1115 ± 27***	1034 ± 30
convex hull	3327 ± 134***	1855 ± 65[n.s.]	3341 ± 118***	3142 ± 119***	1921 ± 56**	1820 ± 66
circularity	0.14 ± 0.01***	0.24 ± 0.01[n.s.]	0.14 ± 0.01***	0.15 ± 0.01***	0.22 ± 0.01[n.s.]	0.23 ± 0.01

[a] Statistical correlations: ***$p < 0.001$, **$p < 0.01$, [n.s.]$p > 0.05$; all calculated against PA **1** group using a two sample Kolmogorov—Smirnov test. [b] Projected cell surface area.

hull, and circularity were performed (a minimum of 200 individual cells were analyzed from two independent experiments for each substrate; Table 1). Projected surface area was found to be ~1.5-fold higher on PA **2** and PA **3**, which contain the RGDS epitope, than on PAs **1** and **4**, which bear no epitope and contain a mutated one, respectively. A similar difference was observed when measuring convex hull, which describes the area enclosed in a polygon obtained by joining the tips of all distal cell processes. We also observed a small but statistically significant difference in both the projected cell area and the convex hull between RGES-bearing PA **4** and non-epitope-bearing PA **1**. However, the absolute values of these measurements are small compared with PA **2** and PA **3**, suggesting a minor effect retained by the scrambled epitope on cell spreading.[60] It is also evident from these data that cell-secreted ECM does not play a major role in this time frame; otherwise, one would not expect the PA epitope to have a significant effect.

In quantifying projected cell surface area and convex hull, we observed a spectrum of cell morphologies, even on a single substrate. Therefore, to better understand the response of the entire cell population, we plotted cumulative frequency distribution against projected cell area (Figure 5B). This style of plot shows every data point (rather than only a mean and a standard deviation) and has the advantage over a traditional bar graph of illustrating trends where a wide data range exists.[61] The plots for PA **2** and PA **3** overlap closely, suggesting that the difference between the photolabile and the control linker have only minor, if any, influence on epitope presentation. Area distributions for PA **1** and PA **4** were also similar, both showing a prominent shift to the left from that of the RGDS-presenting PAs, indicating that cells are less spread on these PAs. We quantified cell roundness by measuring the circularity index, where circularity = $4\pi(\text{area/perimeter}^2)$ (a perfectly circular cell will have an index of 1).[62] A predominant polygonal cell morphology on RGDS epitope-presenting PAs **2** and **3** matches well with the low circularity index observed (0.14 ± 0.01 for both surfaces). Cells exhibited a rounder morphology on surfaces of PAs **1** and **4**, as evidenced by higher circularity indices (0.23 ± 0.01 and 0.22 ± 0.01, respectively).

To examine cell response to PA photolysis, PA-coated surfaces were irradiated prior to cell plating.

Fibroblasts on a surface of irradiated PA **2** were less spread and assumed a round morphology, consistent with the removal of the RGDS epitope. The cumulative distribution plot of projected surface area showed a prominent shift to the left compared with the unirradiated PA **2** condition ($p < 0.001$) and matched closely with RGDS-deficient PA **1** (Figure 5B). Also, the average projected surface area decreased by 33%, and the convex hull was reduced by 44% when substrates were exposed to light. Furthermore, photoirradiation of PA **3** before cell plating did not induce any changes in the cell morphology, confirming that the observed morphological changes were not due to a light-induced change in the supramolecular assembly.

Our results showed that RGDS epitopes on nanofibers facilitated the formation of focal adhesions. To investigate whether this was mediated by an enhanced expression of proteins that comprise focal adhesions, we used quantitative RT-PCR to measure the cellular expression of vinculin and $\beta 1$ integrin, which are known to be recruited in mature focal adhesions.[63] Analyzed at 5 h after plating when differences in both focal adhesion and cell morphology were apparent, we observed similar mRNA expression levels for both proteins regardless of surface coating or irradiation (Figure S4). This result suggests that the observed differences in focal adhesion formation in the presence of RGDS epitopes are primarily mediated by integrin binding and subsequent recruitment of focal adhesion proteins, rather than by an upregulation in protein expression.

Dynamic Cell Response. Distinct cell responses were observed on PA **2** depending on whether or not it was preirradiated. However, to exploit this property to mimic the dynamic nature of native ECM, light-mediated epitope removal needs to be employed while the PA substrate is supporting living cells without causing damage to the cells. To test this possibility, we plated fibroblasts on a coating of PA **2** and allowed the cells to adhere for 1 h. Coatings with adhered cells were then exposed to 365 nm UV light for 10 min to remove the RGDS epitopes from the nanofibers. This amount of exposure to UV light is reported to be well-tolerated by these cells.[13] Consistent with previously reports, we observed partial retraction of the cell process soon after exposure but only minimal associated cell death. More than 90% of the cells were viable immediately after irradiation, and this proportion of live cells was
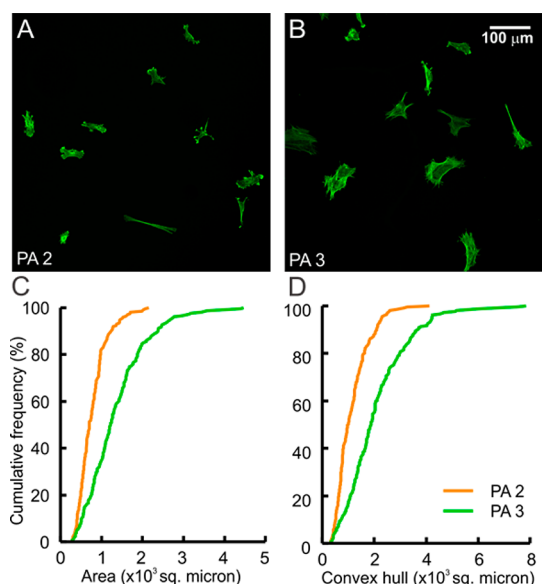
Figure 6. Demonstration of cell response to a dynamic PA substrate. (A,B) Phalloidin-stained images of fibroblasts on a surface of PA **2** (A) and PA **3** (B) after attachment, 10 min irradiation, and 24 h in culture. **(C,D)** Projected surface area (C) and convex hull (D) were found to be significantly lower on PA **2** compared with those on PA **3**.

measurements showed a significant leftward shift for PA **2**, indicating reduced cell spreading (***$p < 0.001$, $n > 195$ cells), with average cell area of 783 ± 25 and $1363 \pm 53 \ \mu m^2$ on PA **2** and PA **3**, respectively. This result confirms that the photolabile residue could be used to dynamically modulate PA bioactivity, with potential to control cellular morphology and development using a light stimulus.

CONCLUSION

We have demonstrated that peptide amphiphile nanofiber matrices can be synthesized by incorporation of a photolabile artificial amino acid to control bioactivity. Through immunostaining and analysis of cell morphology, we showed that cells adhere through integrin-mediated processes onto surfaces displaying PAs that contain the photolabile residue and the bioactive RGDS sequence. Adhesion was dynamically modified by rapid photolytic removal of the RGDS peptide from the supramolecular nanofiber, and control PAs verified the specificity of the RGDS sequence to the observed cell response. Additionally, this method to dynamically control epitope presentation is amenable to cell culture, as cell viability was maintained after exposure to UV light. Most importantly, the incorporation of photolabile groups to generate matrices with light-mediated control over bioactivity and cell behavior is not limited to PAs or to the RGDS sequence, and several other self-assembling peptide-based materials may benefit from this approach. Moreover, peptide sequences that mediate proliferation, differentiation, or other cellular processes may also be used in combination with the photolabile linker described here. We believe that dynamic temporal control of cell–material interactions can become an important component in the design of new artificial matrices based on nanostructures for regenerative medicine research or therapies.

maintained when observed 7 h post-irradiation, eliminating any concerns of UV-induced long-term cytotoxic effects (Figure S5). After 24 h in culture, we found that the cells exhibited a limited capacity for spreading, similar to non-RGDS-bearing substrates (Figure 6A). In contrast, a much higher cell spreading was observed when the cells were seeded on the control PA **3** surface and irradiated following the same protocol (Figure 6B). As before, to better delineate the response of the entire cell population, which has heterogeneous morphologies, we plotted cumulative frequency distribution against projected cell area and convex hull (Figure 6C,D). Both

EXPERIMENTAL SECTION

PA Synthesis. Fmoc-amino acids **I** and **II** syntheses can be found in the Supporting Information. PAs **1**–**5** were synthesized at the Peptide Synthesis Core at the Institute for BioNanotechnology in Medicine. Synthesis of PAs **2**–**4** was performed on a CEM Liberty microwave-assisted peptide synthesizer from Rink amide MBHA resin. PA **5** was synthesized from Biotin Novatag resin. For each coupling, 5 equiv of Fmoc-protected amino acid in DMF was added with 5 equiv of HBTU in DMF and 10 equiv of DIEA in NMP (HBTU = O-benzotriazole-N,N,N',N'-tetramethyluronium hexafluorophosphate; DIEA = N,N-diisopropylethylamine). Fmoc removal was accomplished using a solution of 20% piperidine in DMF and 0.1 M HoBt. Default settings for microwave power and duration were used. The palmitic acid tail was added using the same coupling conditions. The PA was cleaved from the resin in a shaker vessel using a peptide cleavage solution of 95% TFA, 2.5% TIPS, and 2.5% H_2O. Concentration of the cleavage solution *in vacuo* and precipitation of the residue into cold Et_2O afforded the crude product, which was purified by preparative HPLC. MS: PA **2** (M+) calcd 1903.15, found 1903.15; PA **3** (M+) calcd 1827.17, found 1827.08; PA **4** (M+) calcd 1841.18, found 1841.09; PA **5** (M+) calcd

1757.09, found 1757.10. PA **1** was made by photolytic cleavage of PA **2** followed by purification using HPLC. MS: PA **1** (M+) calcd 1207.86, found 1207.89. LCMS traces of PAs **1**–**4**, as well as PA **2** after irradiation for 5 min in a glass capillary, can be found in the Supporting Information.

Transmission Electron Microscopy (TEM). CryoTEM was performed on a JEOL 1230 microscope with an accelerating voltage of 100 kV. A Vitrobot Mark IV equipped with controlled humidity and temperature was used for plunge freezing samples. A small volume (5–10 μL) of PA solution at 0.25% (w/v) in water was deposited on a copper TEM grid with holey carbon support film (EMS, USA) and held in place with tweezers mounted to the Vitrobot. The specimen was blotted in an environment with 90–100% humidity and plunged into a liquid ethane reservoir that was cooled by liquid nitrogen. The vitrified samples were transferred in a nitrogen environment into liquid nitrogen and transferred to a Gatan 626 cryo-holder using a cryo-transfer stage. Samples were imaged using a Gatan 831 bottom-mounted camera.

Labeling with streptavidin gold nanoparticles (AuNPs): A copper TEM grid with carbon support film (EMS, USA) was

placed on a drop (~15 μL) of PA solution (0.1% w/v in water) on a piece of clean parafilm and incubated for 10 min. Excess solution was wicked away with filter paper, and then the grid was rinsed once with Milli-Q water and incubated for 1 h with streptavidin 10 nm AuNPs (Sigma; diluted 1:4 in PBS). After incubation, the samples were gently rinsed three times with Milli-Q water and were negatively stained using a 2% (w/v) uranyl acetate solution in water. Images of negatively stained samples were obtained on a Tecnai Spirit G2 microscope (FEI) operating at 120 kV.

Small-Angle X-ray Scattering (SAXS). Measurements were performed using beamline 5ID-D, in the DuPont—Northwestern—Dow Collaborative Access team (DND-CAT) Synchrotron Research Center at the Advanced Photon Source, Argonne National Laboratory. An energy of 15 keV corresponding to a wavelength $\lambda = 0.83$ Å was selected using a double-crystal monochromator. The data were collected using a CCD detector (MAR) positioned 245 cm behind the sample. The scattering intensity was recorded in the interval $0.005 < q < 0.23$ Å^{-1}. The wave vector was defined as $q = (4\pi/\lambda)\sin(\theta/2)$, where θ is the scattering angle. Samples were lyophilized from HFIP and analyzed in 2 mm quartz capillaries at 0.5% by weight in water. The two-dimensional SAXS images were azimuthally averaged to produce one-dimensional profiles of intensity (*I*) versus *q*, using the two-dimensional data reduction program FIT2D. Scattering of a capillary containing only solvent was also collected and subtracted from the corresponding data. No attempt was made to convert the data to an absolute scale. Detailed methods for SAXS data modeling are provided in the Supporting Information.

Coverslip Coating. Sterile poly-D-lysine-coated glass coverslips (12 mm diameter) were first coated with a thin layer of negatively charged biopolymer sodium alginate (0.25% in Milli-Q water; FMC BioPolymer) and cross-linked with 10 mM aqueous CaCl$_2$ solution. CaCl$_2$ solution was removed and the coverslip was incubated overnight with 0.05% PA solution (in Milli-Q water) at 37 °C. After incubation, the coverslip was gently rinsed once with Milli-Q water, followed by one rinse with DMEM solution. The coverslip surface was never allowed to dry during the entire coating process, and it was left under DMEM until the addition of cells. For 365 nm UV irradiation of the coatings, DMEM was replaced with Dulbecco PBS (containing 1 mM CaCl$_2$), placed inside a Rayonet photoreactor for a designated amount of time, and exposed at an intensity of 9.5 mW/cm^2.

Kinetics Experiments. Coverslips were coated with poly-D-lysine, alginate, and PA **5** (100%) or PA **1** as described above. After UV irradiation, coverslips were washed once with DMSO/PBS (1:1) and once with 1 mM aqueous CaCl$_2$ and then incubated with AlexaFluor-488-conjugated streptavidin for 1 h. The excess streptavidin was removed by washing with PBS (containing 1 mM CaCl$_2$). Fluorescence intensities were recorded on an M5 Spectramax plate reader (Molecular Devices) using the bottom read option with $\lambda_{ex} = 488$ nm and $\lambda_{em} = 520$ nm. The measurement was done at nine points on each coverslip and averaged for each time point ($n = 3$). Background fluorescence was determined from the coverslips ($n = 3$) coated with PA **1** and subtracted from each value. The fluorescence intensity from the 10 min time point was statistically insignificant from the background was not incorporated in the fit. The half-life value was extracted from the first-order kinetics plot.

Cell Culture. NIH 3T3 mouse embryonic fibroblasts were maintained in Dulbecco's modified Eagle's medium (DMEM) with high glucose (GIBCO) supplemented with 10% fetal bovine serum (FBS, Hyclone) and 1% penicillin—streptomycin (P/S) and passaged every 3 days. To study the cell response on PA-coated surfaces, cells were seeded at a low density of 25 cells/mm^2 and incubated for 5 h (37 °C, 5% CO$_2$) under serum-free conditions (DMEM and 1% P/S). The lower cell seeding density was chosen to reduce the chance of cell—cell contact, so that pure cell—substrate interaction could be studied. For dynamic cell response studies, cells were incubated in serum-free media for an hour to facilitate their attachment and spreading on PA surfaces, treated with UV light for 10 min, and then incubated with serum-containing media (DMEM, 10% FBS and 1% P/S) for 24 h.

Fluorescence Staining. Cultured cells were fixed with 4% paraformaldehyde in phosphate buffered saline (PBS) for 15 min at room temperature. The fixing solution and all solutions used in subsequent staining and washing steps were supplemented with 1 mM CaCl$_2$ to prevent dislodgement of the PA coating (which is held on the glass surface by Ca^{2+} cross-linked alginate). Samples were permeabilized and blocked with 0.4% Triton X-100, 10% normal goat serum, and 2% BSA in PBS, followed by overnight incubation with anti-vinculin primary antibody (mouse monoclonal, Sigma; 1:400 dilution) at 4 °C. Primary antibody was detected with AlexaFluor-conjugated secondary antibody (Life Technologies; 1 h incubation at room temperature). Actin filament was visualized by staining with rhodamine or AlexaFluor-488-conjugated phalloidin (Life Technologies; 1:100 dilution, 1 h at room temperature). Cell nuclei were counterstained with DAPI (Life Technologies).

Image Acquisition and Analysis. Images from fluorescently stained samples were acquired using an inverted confocal laser scanning microscope (Nikon A1R) or TissueGnostics cell imaging and analysis system, mounted to an upright microscope (Zeiss). Morphological quantifications were done on phalloidin-stained images of the cells obtained at 20× objective magnification. Acquired images were thresholded using ImageJ software (NIH) and analyzed using routines written in Matlab software (MathWorks). Projected cell surface area was defined by the phalloidin positive pixels occupied by a cell. The convex hull, an index of the cell spread on the substrate, was defined as the total area obtained by joining the tips of most distal processes with straight lines. Shapes of cells were assessed from area and perimeter values by calculating the circularity index, where circularity = 4π(area/perimeter^2). For accurate comparison, quantification of more than 190 randomly selected cells from two independent batches of culture was done for each condition.

Scanning Electron Microscopy (SEM). Cells plated on PA coatings were fixed with 2.5% glutaraldehyde in PBS containing 1 mM CaCl$_2$ (1 h, room temperature) and dehydrated in a graded series of ethanol concentrations. Dehydrated samples (in 100% ethanol) were then dried using a critical point dryer (Tousimis Samdri-795) to preserve structural details. Dried samples were coated with a thin film (14 nm) of osmium metal using an osmium plasma coater (Filgen, OPC-60A) and imaged using a Hitachi S-4800 field emission scanning electron microscope at an accelerating voltage of 5 kV.

Statistical Analysis. Normality of the distribution of cell morphology data sets was tested using the Shapiro-Wilk normality test. A two-sample Kolmogorov—Smirnov test was employed to compare the distribution of morphology parameters between two PA conditions. Data in the table represent mean ± standard error of the mean.

Conflict of Interest: The authors declare no competing financial interest.

Supporting Information Available: SAXS traces and fitting parameters, SEM images, and PCR data, including experimental procedures for each, as well as synthetic details and characterization for new amino acids. This material is available free of charge *via* the Internet at http://pubs.acs.org.

REFERENCES AND NOTES

1. Rozario, T.; DeSimone, D. W. The Extracellular Matrix in Development and Morphogenesis: A Dynamic View. *Dev. Biol.* **2010**, *341*, 126–140.

2. Larsen, M.; Artym, V. V.; Green, J. A.; Yamada, K. M. The Matrix Reorganized: Extracellular Matrix Remodeling and Integrin Signaling. *Curr. Opin. Cell Biol.* **2006**, *18*, 463–471.

3. Calve, S.; Odelberg, S. J.; Simon, H. G. A Transitional Extracellular Matrix Instructs Cell Behavior during Muscle Regeneration. *Dev. Biol.* **2010**, *344*, 259–271.

4. Pierschbacher, M. D.; Ruoslahti, E. Cell Attachment Activity of Fibronectin Can Be Duplicated by Small Synthetic Fragments of the Molecule. *Nature* **1984**, *309*, 30–33.

5. Tashiro, K.; Sephel, G. C.; Weeks, B.; Sasaki, M.; Martin, G. R.; Kleinman, H. K.; Yamada, Y. A Synthetic Peptide Containing the IKVAV Sequence from the a-Chain of Laminin Mediates Cell Attachment, Migration, and Neurite Outgrowth. *J. Biol. Chem.* **1989**, *264*, 16174–16182.

6. Hersel, U.; Dahmen, C.; Kessler, H. RGD Modified Polymers: Biomaterials for Stimulated Cell Adhesion and Beyond. *Biomaterials* **2003**, *24*, 4385–4415.

7. Shin, H.; Jo, S.; Mikos, A. G. Biomimetic Materials for Tissue Engineering. *Biomaterials* **2003**, *24*, 4353–4364.

8. Hartgerink, J. D.; Beniash, E.; Stupp, S. I. Self-Assembly and Mineralization of Peptide-Amphiphile Nanofibers. *Science* **2001**, *294*, 1684–1688.

9. Silva, G. A.; Czeisler, C.; Niece, K. L.; Beniash, E.; Harrington, D. A.; Kessler, J. A.; Stupp, S. I. Selective Differentiation of Neural Progenitor Cells by High-Epitope Density Nanofibers. *Science* **2004**, *303*, 1352–1355.

10. Sur, S.; Pashuck, E. T.; Guler, M. O.; Ito, M.; Stupp, S. I.; Launey, T. A Hybrid Nanofiber Matrix To Control the Survival and Maturation of Brain Neurons. *Biomaterials* **2012**, *33*, 545–555.

11. Daley, W. P.; Peters, S. B.; Larsen, M. Extracellular Matrix Dynamics in Development and Regenerative Medicine. *J. Cell Sci.* **2008**, *121*, 255–264.

12. Matson, J. B.; Stupp, S. I. Self-Assembling Peptide Scaffolds for Regenerative Medicine. *Chem. Commun.* **2012**, *48*, 26–33.

13. Kloxin, A. M.; Kasko, A. M.; Salinas, C. N.; Anseth, K. S. Photodegradable Hydrogels for Dynamic Tuning of Physical and Chemical Properties. *Science* **2009**, *324*, 59–63.

14. Matson, J. B.; Zha, R. H.; Stupp, S. I. Peptide Self-Assembly for Crafting Functional Biological Materials. *Curr. Opin. Solid State Mater. Sci.* **2011**, *15*, 225–235.

15. Hauser, C. A. E.; Zhang, S. G. Designer Self-Assembling Peptide Nanofiber Biological Materials. *Chem. Soc. Rev.* **2010**, *39*, 2780–2790.

16. Nagarkar, R. P.; Hule, R. A.; Pochan, D. J.; Schneider, J. P. Domain Swapping in Materials Design. *Biopolymers* **2010**, *94*, 141–155.

17. Webber, M. J.; Kessler, J. A.; Stupp, S. I. Emerging Peptide Nanomedicine To Regenerate Tissues and Organs. *J. Intern. Med.* **2010**, *267*, 71–88.

18. Collier, J. H.; Rudra, J. S.; Gasiorowski, J. Z.; Jung, J. P. Multi-Component Extracellular Matrices Based on Peptide Self-Assembly. *Chem. Soc. Rev.* **2010**, *39*, 3413–3424.

19. Yu, Y. C.; Berndt, P.; Tirrell, M.; Fields, G. B. Self-Assembling Amphiphiles for Construction of Protein Molecular Architecture. *J. Am. Chem. Soc.* **1996**, *118*, 12515–12520.

20. Hartgerink, J. D.; Beniash, E.; Stupp, S. I. Peptide-Amphiphile Nanofibers: A Versatile Scaffold for the Preparation of Self-Assembling Materials. *Proc. Natl. Acad. Sci. U.S.A.* **2002**, *99*, 5133–5138.

21. Velichko, Y. S.; Stupp, S. I.; de la Cruz, M. O. Molecular Simulation Study of Peptide Amphiphile Self-Assembly. *J. Phys. Chem. B* **2008**, *112*, 2326–2334.

22. Storrie, H.; Guler, M. O.; Abu-Amara, S. N.; Volberg, T.; Rao, M.; Geiger, B.; Stupp, S. I. Supramolecular Crafting of Cell Adhesion. *Biomaterials* **2007**, *28*, 4608–4618.

23. Webber, M. J.; Tongers, J.; Renault, M. A.; Roncalli, J. G.; Losordo, D. W.; Stupp, S. I. Development of Bioactive Peptide Amphiphiles for Therapeutic Cell Delivery. *Acta Biomater.* **2010**, *6*, 3–11.

24. Webber, M. J.; Han, X. Q.; Murthy, S. N. P.; Rajangam, K.; Stupp, S. I.; Lomasney, J. W. Capturing the Stem Cell Paracrine Effect Using Heparin-Presenting Nanofibres To Treat Cardiovascular Diseases. *J. Tissue Eng. Regener. Med.* **2010**, *4*, 600–610.

25. Webber, M. J.; Tongers, J.; Newcomb, C. J.; Marquardt, K.-T.; Bauersachs, J.; Losordo, D. W.; Stupp, S. I. Supramolecular Nanostructures That Mimic VEGF as a Strategy for Ischemic Tissue Repair. *Proc. Natl. Acad. Sci. U.S.A.* **2011**, *108*, 13438–13443.

26. Tysseling-Mattiace, V. M.; Sahni, V.; Niece, K. L.; Birch, D.; Czeisler, C.; Fehlings, M. G.; Stupp, S. I.; Kessler, J. A. Self-Assembling Nanofibers Inhibit Glial Scar Formation and Promote Axon Elongation after Spinal Cord Injury. *J. Neurosci.* **2008**, *28*, 3814–3823.

27. Angeloni, N. L.; Bond, C. W.; Tang, Y.; Harrington, D. A.; Zhang, S. M.; Stupp, S. I.; McKenna, K. E.; Podlasek, C. A. Regeneration of the Cavernous Nerve by Sonic Hedgehog Using Aligned Peptide Amphiphile Nanofibers. *Biomaterials* **2011**, *32*, 1091–1101.

28. Bond, C. W.; Angeloni, N. L.; Harrington, D. A.; Stupp, S. I.; McKenna, K. E.; Podlasek, C. A. Peptide Amphiphile Nanofiber Delivery of Sonic Hedgehog Protein To Reduce Smooth Muscle Apoptosis in the Penis after Cavernous Nerve Resection. *J. Sex. Med.* **2011**, *8*, 78–89.

29. Matson, J. B.; Stupp, S. I. Drug Release from Hydrazone-Containing Peptide Amphiphiles. *Chem. Commun.* **2011**, *47*, 7962–7964.

30. Matson, J. B.; Newcomb, C. J.; Bitton, R.; Stupp, S. I. Nanostructure-Templated Control of Drug Release from Peptide Amphiphile Nanofiber Gels. *Soft Matter* **2012**, *8*, 3586–3595.

31. Webber, M. J.; Newcomb, C. J.; Bitton, R.; Stupp, S. I. Switching of Self-Assembly in a Peptide Nanostructure with a Specific Enzyme. *Soft Matter* **2011**, *7*, 9665–9672.

32. Soukasene, S.; Toft, D. J.; Moyer, T. J.; Lu, H.; Lee, H.-K.; Standley, S. M.; Cryns, V. L.; Stupp, S. I. Antitumor Activity of Peptide Amphiphile Nanofiber-Encapsulated Camptothecin. *ACS Nano* **2011**, *5*, 9113–9121.

33. Matson, J. B.; Webber, M. J.; Tamboli, V. K.; Weber, B.; Stupp, S. I. A Peptide-Based Material for Therapeutic Carbon Monoxide Delivery. *Soft Matter* **2012**, *8*, 2689–2692.

34. Webber, M. J.; Matson, J. B.; Tamboli, V. K.; Stupp, S. I. Controlled Release of Dexamethasone from Peptide Nanofiber Gels To Modulate Inflammatory Response. *Biomaterials* **2012**, *33*, 6823–6832.

35. Standley, S. M.; Toft, D. J.; Cheng, H.; Soukasene, S.; Chen, J.; Raja, S. M.; Band, V.; Band, H.; Cryns, V. L.; Stupp, S. I. Induction of Cancer Cell Death by Self-Assembling Nanostructures Incorporating a Cytotoxic Peptide. *Cancer Res.* **2010**, *70*, 3020–3026.

36. Mata, A.; Geng, Y. B.; Henrikson, K. J.; Aparicio, C.; Stock, S. R.; Satcher, R. L.; Stupp, S. I. Bone Regeneration Mediated by Biomimetic Mineralization of a Nanofiber Matrix. *Biomaterials* **2010**, *31*, 6004–6012.

37. Spoerke, E. D.; Anthony, S. G.; Stupp, S. I. Enzyme Directed Templating of Artificial Bone Mineral. *Adv. Mater.* **2009**, *21*, 425–430.

38. Shah, R. N.; Shah, N. A.; Lim, M. M. D.; Hsieh, C.; Nuber, G.; Stupp, S. I. Supramolecular Design of Self-Assembling Nanofibers for Cartilage Regeneration. *Proc. Natl. Acad. Sci. U.S.A.* **2010**, *107*, 3293–3298.

39. Huang, Z.; Newcomb, C. J.; Bringas, P., Jr.; Stupp, S. I.; Snead, M. L. Biological Synthesis of Tooth Enamel Instructed by an Artificial Matrix. *Biomaterials* **2010**, *31*, 9202–9211.

40. Yang, Z. M.; Gu, H. W.; Fu, D. G.; Gao, P.; Lam, J. K.; Xu, B. Enzymatic Formation of Supramolecular Hydrogels. *Adv. Mater.* **2004**, *16*, 1440–1444.

41. Williams, R. J.; Smith, A. M.; Collins, R.; Hodson, N.; Das, A. K.; Ulijn, R. V. Enzyme-Assisted Self-Assembly under Thermodynamic Control. *Nat. Nanotechnol.* **2009**, *4*, 19–24.

42. Madsen, J.; Armes, S. P.; Bertal, K.; Lomas, H.; MacNeil, S.; Lewis, A. L. Biocompatible Wound Dressings Based on Chemically Degradable Triblock Copolymer Hydrogels. *Biomacromolecules* **2008**, *9*, 2265–2275.

43. Muraoka, T.; Cui, H.; Stupp, S. I. Quadruple Helix Formation of a Photoresponsive Peptide Amphiphile and Its Light-Triggered Dissociation into Single Fibers. *J. Am. Chem. Soc.* **2008**, *130*, 2946–2947.

44. Muraoka, T.; Koh, C. Y.; Cui, H. G.; Stupp, S. I. Light-Triggered Bioactivity in Three Dimensions. *Angew. Chem., Int. Ed.* **2009**, *48*, 5946–5949.

45. Luo, Y.; Shoichet, M. S. A Photolabile Hydrogel for Guided Three-Dimensional Cell Growth and Migration. *Nat. Mater.* **2004**, *3*, 249–253.

46. DeForest, C. A.; Anseth, K. S. Cytocompatible Click-Based Hydrogels with Dynamically Tunable Properties through Orthogonal Photoconjugation and Photocleavage Reactions. *Nat. Chem.* **2011**, *3*, 925–931.

47. Johnson, J. A.; Lewis, D. R.; Az, D.; Finn, M. G.; Koberstein, J. T.; Turro, N. J. Synthesis of Degradable Model Networks *via* ATRP and Click Chemistry. *J. Am. Chem. Soc.* **2006**, *128*, 6564–6565.

48. Holmes, C. P. Model Studies for New *O*-Nitrobenzyl Photolabile Linkers: Substituent Effects on the Rates of Photochemical Cleavage. *J. Org. Chem.* **1997**, *62*, 2370–2380.

49. Ramos, R.; Manning, B.; Avino, A.; Gargallo, R.; Eritja, R. Photocleavage of Peptides and Oligodeoxynucleotides Carrying 2-Nitrobenzyl Groups. *Helv. Chim. Acta* **2009**, *92*, 613–622.

50. Loewik, D. W. P. M.; Meijer, J. T.; Minten, I. J.; Van Kalkeren, H.; Heckenmuller, L.; Schulten, I.; Sliepen, K.; Smittenaar, P.; Van Hest, J. C. M. Controlled Disassembly of Peptide Amphiphile Fibres. *J. Pept. Sci.* **2008**, *14*, 127–133.

51. Fomina, N.; McFearin, C.; Sermsakdi, M.; Edigin, O.; Almutairi, A. UV and Near-IR Triggered Release from Polymeric Nanoparticles. *J. Am. Chem. Soc.* **2010**, *132*, 9540–9542.

52. Fmoc-amino acid **I** was also synthesized without the nitro group but was found to be unstable in TFA, necessitating the redesign of the Fmoc-amino acid to linker stable **II**.

53. Capito, R. M.; Azevedo, H. S.; Velichko, Y. S.; Mata, A.; Stupp, S. I. Self-Assembly of Large and Small Molecules into Hierarchically Ordered Sacs and Membranes. *Science* **2008**, *319*, 1812–1816.

54. Grafahrend, D.; Heffels, K.-H.; Beer, M. V.; Gasteier, P.; Moeller, M.; Boehm, G.; Dalton, P. D.; Groll, J. Degradable Polyester Scaffolds with Controlled Surface Chemistry Combining Minimal Protein Adsorption with Specific Bioactivation. *Nat. Mater.* **2011**, *10*, 67–73.

55. Massia, S. P.; Hubbell, J. A. An RGD Spacing of 440 nm Is Sufficient for Integrin $\alpha v \beta 3$-Mediated Fibroblast Spreading and 140 nm for Focal Contact and Stress Fiber Formation. *J. Cell Biol.* **1991**, *114*, 1089–1100.

56. Schvartzman, M.; Palma, M.; Sable, J.; Abramson, J.; Hu, X.; Sheetz, M. P.; Wind, S. J. Nanolithographic Control of the Spatial Organization of Cellular Adhesion Receptors at the Single-Molecule Level. *Nano Lett.* **2011**, *11*, 1306–1312.

57. Gasiorowski, J. Z.; Collier, J. H. Directed Intermixing in Multicomponent Self-Assembling Biomaterials. *Biomacromolecules* **2011**, *12*, 3549–3558.

58. Jung, J. P.; Nagaraj, A. K.; Fox, E. K.; Rudra, J. S.; Devgun, J. M.; Collier, J. H. Co-assembling Peptides as Defined Matrices for Endothelial Cells. *Biomaterials* **2009**, *30*, 2400–2410.

59. Zhang, S.; Holmes, T. C.; DiPersio, C. M.; Hynes, R. O.; Su, X.; Rich, A. Self-Complementary Oligopeptide Matrices Support Mammalian Cell Attachment. *Biomaterials* **1995**, *16*, 1385–1393.

60. Dsouza, S. E.; Ginsberg, M. H.; Plow, E. F. Arginyl-Glycyl-Aspartic Acid (RGD)—A Cell-Adhesion Motif. *Trends. Biochem. Sci.* **1991**, *16*, 246–250.

61. Cingolani, L. A.; Thalhammer, A.; Yu, L. M. Y.; Catalano, M.; Ramos, T.; Colicos, M. A.; Goda, Y. Activity-Dependent Regulation of Synaptic AMPA Receptor Composition and Abundance by $\beta 3$ Integrins. *Neuron* **2008**, *58*, 749–762.

62. Sung, K. E.; Yang, N.; Pehlke, C.; Keely, P. J.; Eliceiri, K. W.; Friedl, A.; Beebe, D. J. Transition to Invasion in Breast Cancer: A Microfluidic *In Vitro* Model Enables Examination of Spatial and Temporal Effects. *Int. J. Integr. Biol.* **2011**, *3*, 439–450.

63. Puklin-Faucher, E.; Sheetz, M. P. The Mechanical Integrin Cycle. *J. Cell Sci.* **2009**, *122*, 179–186.